Noname manuscript No.
(will be inserted by the editor)

Large-Eddy Simulation of the Atmospheric Boundary Layer with Near-Wall Resolved Turbulence

Livia S. Freire

Received: DD Month YEAR / Accepted: DD Month YEAR

Abstract

In this study, a Large-Eddy Simulation (LES) code with the One-Dimensional Turbulence (ODT) wall model is tested for the simulation of the atmospheric boundary layer under neutral, stable, unstable and free-convection conditions. ODT provides a vertically refined flow field near the wall, which has small-scale fluctuations from the ODT stochastic turbulence model and an extension of the LES large-scale coherent structures. From this additional field, the lower boundary conditions needed by LES can be extracted. Results are compared to the LES using the classical algebraic wall model based on the Monin-Obukhov Similarity Theory (MOST), showing similar results in most of the domain with improvements in horizontal velocity and temperature spectra in the near-wall region for simulations of the neutral/stable/unstable cases. For the free-convection test, spectra from the ODT part of the flow were directly compared to spectra generated by LES-MOST at the same height, showing similar behavior despite some degradation. Furthermore, the additional flow field improved the near-wall vertical velocity skewness for the unstable/free-convection cases. The tool is demonstrated to provide adequate results without the need of any case-specific parameter tuning. Future studies involving complex physicochemical processes at the surface (such as the presence of vertically distributed sources and sinks of matter and energy) within a large domain are likely to benefit from this tool.

Keywords Atmospheric boundary layer · Large-Eddy Simulation · Near-wall turbulence · One-Dimensional Turbulence · Stochastic wall model

Livia S. Freire
Instituto de Ciências Matemáticas e de Computação, University of São Paulo, São Carlos, Brazil
E-mail: liviafreire@usp.br

1 Introduction

Many physical phenomena of interest in the atmospheric boundary layer (ABL) happen in the first few meters above ground, being directly impacted by the interaction between the flow field and the elements of the surface. Examples include the exchange of gases and particles with vegetation, the pollution emitted within cities, the wind-energy production, the *saltation* (jump) of sand particles causing the emission of dust, the presence of breaking waves or dunes, and many others. These phenomena can modify significantly the flow field, impacting not only the mean wind but also the structure of turbulence (Finnigan 2000; Andreotti et al. 2009; Kok et al. 2012; Giometto et al. 2016; Sullivan et al. 2018; Chen et al. 2019), therefore requiring specialized tools in order to properly investigate their characteristics.

Given the highly turbulent nature of the flow and the wide range of scales present in the ABL, the Large-Eddy Simulation (LES) has been the main tool used in its numerical investigation (Stoll et al. 2020). However, as LES typically has a fixed grid size (e.g. Kleissl et al. 2006; Freire et al. 2016; Salesky and Anderson 2018) or a gentle grid stretching in the vertical direction (e.g. Sullivan et al. 2018; Bhuiyan and Alam 2020; Wurps et al. 2020), the simulation of the first few centimeters in a domain in the order of one kilometer (the scale of the ABL height) has a prohibitive computational cost. For that reason, most studies interested in the near-wall flow had to restrict the domain to a fraction of the ABL (e.g. Dupont et al. 2013, 2014; Pan et al. 2014, 2015; Zhong et al. 2017; Han et al. 2018; Zhang et al. 2018; Richter et al. 2019), and consequently they are usually limited to the neutral atmospheric surface layer. Since the near-wall region can be impacted by wall-turbulence coherent structures that require the simulation of the entire ABL under different atmospheric stabilities (as in Khanna and Brasseur 1997, 1998; Salesky and Anderson 2018, 2020, for example), alternatives to this numerical limitation are necessary.

In this study, the use of the LES-ODT model (Freire and Chamecki 2021) is tested in the context of a flat ABL with different stabilities. This tool corresponds to a traditional LES model with fixed grid size, similar to the open-source code LESGO (Kleissl et al. 2006; Yang et al. 2017; Salesky and Anderson 2018). The original wall model corresponds to an algebraic equation based on the Monin-Obukhov Similarity Theory (MOST), an extension of the logarithmic law-of-the-wall that provides adequate results for a wide range of atmospheric stabilities (Kleissl et al. 2006; Freire et al. 2016; Salesky and Anderson 2020). When coupled to LES, the One-Dimensional Turbulence model (ODT) provides a vertically refined flow field within the lowest LES grid layer, which has turbulence-like small-scale fluctuations (provided by a stochastic turbulence model), superimposed on the LES-driven large-scale flow. Since a resolved flow field is provided, ODT can be used to calculate the lower boundary conditions needed by LES, therefore replacing the MOST-based ones. Furthermore, the resolved flow can be used to improve the representation of turbulence interaction with various near-wall physical and chemical processes,

such as those present in vegetation and cities, which will be the focus of future investigation with this tool.

The ODT model was developed by Kerstein (1999) and used as a stand-alone model to simulate different types of turbulent flows in a 1D domain, including homogeneous turbulence, shear layers and buoyant flows in the original study, mixing layer and a wake by Kerstein et al. (2001), jet diffusion flames (Echekki et al. 2001), the stable ABL (Kerstein and Wunsch 2006), particle dispersion in homogeneous flow (Sun et al. 2014), scalar transport in channel flows (Klein and Schmidt 2018), developing boundary layers (Rakhi et al. 2019) and heated channel flow (Klein et al. 2022). In addition, ODT was coupled to LES and used to represent the viscous and buffer layers of smooth channel flows for different Reynolds numbers (Schmidt et al. 2003).

In an effort to obtain a version of the code suitable for ABL simulation without case-specific parameter tuning, Freire and Chamecki (2018) developed new subgrid and wall models for ODT, obtaining satisfactory results in the simulation of the unstable ABL in the presence of plant canopies. This new code version was also coupled to LES, and the simulation of smooth and rough channels were validated for different LES subgrid-scale models, Reynolds numbers and grid resolutions (Freire and Chamecki 2021). In the present study, the code is expanded to simulate the stratified ABL by incorporating the Coriolis and buoyancy forces, with particular attention to the latter due to its complex representation in ODT (as a potential energy in the stochastic turbulence model). Finally, given that the tool is still relatively unconventional (compared to LES using MOST wall model, hereafter LES-MOST, for example), this study aims at validating this new code setup before applying it to future studies involving complex near-wall phenomena.

The LES-ODT model is described in details in Sec. 2, and it is used to simulate examples of neutral, stable and unstable ABL based on the cases from Kleissl et al. (2006), in addition to a free-convection case from Salesky and Anderson (2018) (cases described in Sec. 3). All results are presented using LES-MOST as a reference, and a discussion regarding the cost-benefit of the LES-ODT model is given in Sec. 4. Concluding remarks are given in Sec. 5.

2 The LES-ODT model

The two-way coupling between the LES and ODT models can be better described by breaking it into four different regions, as listed in Tab. 1. While the bulk of the simulation is provided by LES in the traditional way, the near-wall region (comprising the lower layer of grid cells) is resolved by a “forest” of ODT models (vertical 1D domains) plus advective transfers between them (driven by LES-scale velocities). On top of the ODT domain, there is an overlap region in which the LES vertical fluxes are complemented by fluxes from the ODT stochastic turbulence model. Finally, the ODT interaction with the wall is modeled through a ODT wall model (in here based on the logarithmic law-of-the-wall). Details of this model hierarchy are given next.

Table 1 Hierarchy of the LES-ODT model and its domain regions

Region	model used	# of LES vertical grid cells
bulk	LES	$nz-1$
overlap region	LES + stochastic eddy fluxes	2.5
near-wall	ODT + LES-scale advection	1
wall	ODT wall model	–

2.1 The LES model

The LES code used here solves the filtered Navier–Stokes equation in divergence form (Freire and Chamecki 2021) and the filtered transport equation for potential temperature, written as (using traditional index notation)

$$\frac{\partial \widetilde{U}_i}{\partial x_i} = 0, \tag{1}$$

$$\frac{\partial \widetilde{U}_i}{\partial t} + \frac{\partial \widetilde{U}_i \widetilde{U}_j}{\partial x_j} = -\frac{\partial \widetilde{P}}{\partial x_i} + f[\widetilde{U}_2 - V_g]\delta_{i1} - f[\widetilde{U}_1 - U_g]\delta_{i2} - g\frac{\widetilde{\Theta}'}{\Theta_0}\delta_{i3} - \frac{\partial \tau_{ij}}{\partial x_j}, \tag{2}$$

$$\frac{\partial \widetilde{\Theta}}{\partial t} + \frac{\partial \widetilde{\Theta}\widetilde{U}_j}{\partial x_j} = -\frac{\partial q_j}{\partial x_j}, \tag{3}$$

where $\widetilde{U}_i$, $\widetilde{P}$ and $\widetilde{\Theta}$ are the velocity, modified pressure and potential temperature fields resolved in the LES grid, t is time and x_i is the position vector (u, v, w and x, y, z are also used for convenience). The potential temperature field behaves as an active scalar, creating vertical accelerations through the use of the Boussinesq approximation (fourth term on the RHS of Eq. (2), in which $\widetilde{\Theta}'$ is the deviation from the horizontal planar average Θ_0 and g is the gravitational acceleration). The flow is driven by a mean constant pressure gradient in geostrophic balance above the ABL (where a temperature inversion suppresses turbulence), which is imposed through a Coriolis force in the horizontal directions (second and third terms in the RHS of Eq. (2), where f is the Coriolis parameter and U_g, V_g are the horizontal components of the geostrophic wind). The effect of the unresolved part of the flow is accounted for by the subgrid scale (SGS) deviatoric shear stress tensor τ_{ij} and temperature flux q_j, which are modeled using the Prandtl's mixing length hypothesis as $\tau_{ij} = -2\nu_{sgs}\widetilde{S}_{ij}$ and $q_j = -(\nu_{sgs}/Pr_{sgs})(\partial\widetilde{\Theta}/\partial x_j)$, where ν_{sgs} is the SGS eddy viscosity, Pr_{sgs} is the SGS Prandtl number and $\widetilde{S}_{ij}$ is the resolved strain-rate tensor. In here, Pr_{sgs} is assumed constant and equal to 0.4 as in the reference simulations of Kleissl et al. (2006) and Salesky and Anderson (2018). The eddy viscosity parameter is obtained from the Lagrangian-averaged scale-dependent dynamic model as described by Bou-Zeid et al. (2005). The modified pressure $\widetilde{P} = \widetilde{p}/\rho_0 + \tau_{ii}/3 + \widetilde{u}_i\widetilde{u}_i/2$ (where $\widetilde{p}$ is the dynamic pressure and ρ_0 is the fluid density) is used to impose the divergence-free condition on the flow, computed as usual from a Poisson equation.

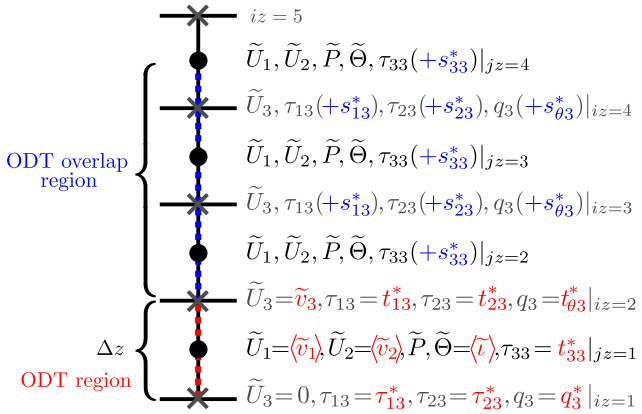

Fig. 1 Vertically staggered positions of variables in the LES (black and grey) indicated by crosses (index iz) and circles (index jz). ODT region in red (ODT variables in red replaces the original LES values) and ODT overlap region in blue (ODT variables in blue are added to the corresponding LES variables).

A Cartesian, vertically staggered grid with fixed size is used (Fig. 1), and the numerical solution uses a fully dealiased pseudo-spectral method in the horizontal directions, a second-order centered finite-difference in the vertical direction and a fully explicit second-order Adams–Bashforth scheme for time integration. Horizontal boundary conditions are periodic, and a stress-free boundary condition with zero vertical velocity is applied at the top of the domain. A sponge layer is also added to the uppermost quarter of the vertical domain, which uses a relaxation term that damps fluctuations in order to dissipate energy of gravity waves (Nieuwstadt et al. 1991).

Due to the staggered grid configuration (Fig. 1), the values of $\widetilde{U}_3, \tau_{13}, \tau_{23}$ and q_3 at the wall need to be defined as bottom boundary conditions. Constant values of heat flux q_3 are prescribed (see values in Sec 3), as well as $\widetilde{U}_3 = 0$. For the wall shear stress, the traditional approach of using MOST is reproduced here as a reference (LES-MOST cases), defined as

$$\tau_{i3}|_{iz=1} = -\left[\frac{\kappa}{\ln(z^*/z_0) - \psi_m(z^*/L)}\right]^2 (\widehat{U}_1^2 + \widehat{U}_2^2)^{1/2} \widehat{U}_i, \quad i = 1, 2, \tag{4}$$

in which κ is the Von Kármán constant, $z^* = \Delta z/2$ is the lowest height at which the horizontal velocities are defined, z_0 is the surface roughness length scale, L is the Obukhov length, $\psi_m(z/L) = \int_{z_0/L}^{z/L} [1 - \phi_m(x)]dx/x$ is the momentum stability function (calculated from the nondimensional velocity gradient ϕ_m) and $\widehat{U}_i$ are the resolved horizontal velocities at z^* ($jz = 1$), filtered at the scale 2Δ to compensate for the log-law mismatch of the mean velocity gradient (Bou-Zeid et al. 2005; Yang et al. 2017). The nondimensional velocity

gradients used here correspond to (Kaimal and Finnigan 1994)

$$\phi_m(z/L) = \frac{\kappa z}{u_*}\frac{d\widehat{U}}{dz} = \begin{cases} (1-16z/L)^{-1/4}, & L<0, \\ (1+4.8z/L), & L>0, \\ 1, & L=0. \end{cases} \tag{5}$$

Note that for the neutral ABL ($L = 0$), this corresponds to the logarithmic law from the classical law-of-the-wall tested in the neutral channel flow cases of Freire and Chamecki (2021). For LES-ODT, $\tau_{i3}|_{iz=1}$ are instead obtained from ODT.

2.2 The ODT model

The ODT model is designed to provide the flow statistics along a line of sight within a 3D turbulent flow. It corresponds to a one-dimensional diffusion equation, combined with a stochastic turbulence model that represents the three-dimensional advection term in a 1D domain. The advancement equations of the ODT region of the flow (Tab. 1 and Fig. 1), can be written as

$$\frac{\partial \widetilde{u}_i}{\partial t} + \frac{\partial \widetilde{u}_i\widetilde{v}_j}{\partial x_j} = f[\widetilde{u}_2 - V_g]\delta_{i1} - f[\widetilde{u}_1 - U_g]\delta_{i2} - \frac{\partial \tau^*_{i3}}{\partial x_3} + \textit{eddy events}, \tag{6}$$

$$\frac{\partial \widetilde{\theta}}{\partial t} + \frac{\partial \widetilde{\theta}\widetilde{v}_j}{\partial x_j} = -\frac{\partial q^*_3}{\partial x_3} + \textit{eddy events}, \tag{7}$$

in which x_3 is the vertical direction, $\widetilde{u}_i$ and $\widetilde{\theta}$ are the velocity vector and potential temperature resolved in the ODT grid, $\tau^*_{i3} = \nu^*_{sgs}\partial\widetilde{u}_i/\partial x_3$ and $q^*_3 = (\nu^*_{sgs}/Pr_{sgs})(\partial\widetilde{\theta}/\partial x_3)$ are the ODT subgrid-scale vertical momentum and heat fluxes, ν^*_{sgs} is the SGS eddy-viscosity in the ODT scale (calculated from a constant Smagorinsky SGS model with wall-damping function as in Freire and Chamecki 2018, 2021), and $Pr_{sgs} = 0.4$ is used as in the LES code. Note that in this approach ODT is also in "large-eddy" mode, i.e., it does not resolve the flow down to the viscous scale, instead the equations are filtered at the ODT grid scale. For that reason, the molecular viscosity and diffusivity are neglected, as they are small compared to their SGS counterparts. Furthermore, the advection terms (second terms in the LHS of Eqs. (6) and (7)), which are not present in the ODT stand-alone formulation, represent the advection from a LES-scale velocity that connects adjacent ODT domains and will be described in the next section.

The *eddy events* are prescribed by a stochastic model that mimics the turbulent transport effects that are otherwise missing in Eqs. (6) and (7), as well as dynamic pressure and buoyancy effects that are otherwise missing in Eqs. (6). When stochastic eddies are selected, they act instantaneously in the flow field by replacing the variables of the flow as follows:

$$\widetilde{u}_i(z) \rightarrow \widetilde{u}_i(M(z)) + c_i K(z), \tag{8}$$

$$\widetilde{\theta}(z) \rightarrow \widetilde{\theta}(M(z)), \tag{9}$$

in which $M(z)$ represents a mapping function, and $K(z)$ is a kernel function that modifies the amount and spatial distribution of the kinetic energy of individual velocity components. The mapping function is a model for advection based on a triplet map, which "takes a line segment, shrinks it to a third of its original length, and then places three copies on the original domain; the middle copy is reversed, which maintains continuity of advected fields and introduces the rotational folding effect of turbulent eddy motion" (Kerstein and Wunsch 2006). Its mathematical formulation is given by

$$M(z) = z_b + \begin{cases} 3(z - z_b), & \text{if } z_b \le z \le (z_b + l/3), \\ 2l - 3(z - z_b), & \text{if } (z_b + l/3) \le z \le (z_b + 2l/3), \\ 3(z - z_b) - 2l, & \text{if } (z_b + 2l/3) \le z \le (z_b + l), \\ z - z_b, & \text{otherwise,} \end{cases} \tag{10}$$

where l and z_b are the eddy size and bottom position, respectively (Kerstein et al. 2001). This formulation preserves the total amount of the quantity being transported, and it mimics the turbulence energy cascade by transferring energy from large to small scales.

The additional term $c_i K(z)$ in Eq. (8) induces redistribution of energy among velocity components, mimicking a pressure-induced tendency towards isotropy on the flow. The kernel function $K(z) = [z - M(z)]$ is the distance that the fluid parcel is displaced during an eddy event, and

$$c_i = \frac{27}{4l}\left[-u_{i,K} \pm \sqrt{\frac{1}{3}\left(u_{1,K}^2 + u_{2,K}^2 + u_{3,K}^2 + \frac{8gl}{27}\frac{\theta_K}{\theta_0}\right)}\right] \tag{11}$$

is the amplitude of energy redistribution. The quantity inside the parenthesis represents the total amount of energy available for redistribution (kinetic plus potential), in which

$$n_K \equiv \frac{1}{l^2}\int_{z_b}^{z_b+l} \widetilde{n}(M(z))K(z)dz \tag{12}$$

for $n = u_i$ or θ. The sign ambiguity in Eq. (11) corresponds to the sign of $u_{i,K}$ (Kerstein et al. 2001).

The combination of the triplet map with the energy redistribution embodies the salient phenomenology of turbulent flows. The final piece of information needed to close the model is the selection criterion of *eddy events*, which is obtained from a probability distribution of eddy size l and location z_b in the form

$$\lambda(z_b, l; t) = \frac{C_\lambda}{l^3}\sqrt{\frac{1}{3}\left(u_{1,K}^2 + u_{2,K}^2 + u_{3,K}^2 + \frac{8gl}{27}\frac{\theta_K}{\theta_0}\right)}. \tag{13}$$

This distribution, constructed from dimensional arguments (Kerstein and Wunsch 2006), uses the instantaneous amount of kinetic and potential energy in the flow (through the n_K values), adding another physical aspect to the stochastic

model. The constant C_λ, which is the only tunable parameter in this version of the code, regulates the frequency of eddy occurrences for a given amount of energy, setting the turbulence intensity. Its value is typically in the order of 10, and small adjustments are usually performed for different types of flows. For LES-ODT of smooth and rough channel flows, Freire and Chamecki (2021) used $C_\lambda = 15$, for all values of Reynolds number and grid resolution. This C_λ value is also adopted here without any fine-tuning to emphasize the robustness of the code, in particular of the potential energy representation.

In LES-ODT, the ODT model has a domain corresponding to the lowest grid cells of the LES (Δz), and a mesh with fixed size corresponding to a fraction of the LES vertical grid cell ($\Delta_{\mathrm{ODT}} = \Delta z / n_{\mathrm{ODT}}$, where n_{ODT} is the number of ODT grid points). The variables in ODT are collocated at the nodes, and the lower boundary condition comes from a log-law wall model similar to what is typically performed in LES (see details in Freire and Chamecki 2021). This approach is repeated at each LES cell adjacent to the wall, creating a "forest" of $nx \times ny$ ODT vertical lines (nx and ny are the number of LES cells in the two horizontal directions). Although individual ODT lines are mostly independent of each other during their 1D advancement, each of them is advected by velocities in LES scale (advection terms in Eqs. (6) and (7)), as will be described next.

The ODT model is solved explicitly using forward Euler method for the time discretization and a first-order forward finite difference for the vertical derivatives. Initially, $\Delta t_{\mathrm{ODT}} = \Delta t_{\mathrm{LES}}/15$ and it can be decreased by successive factors of 2 during the simulation depending on the frequency of *eddy events*. This is because the eddy distribution calculation uses a statistical approximation known as the "rejection method" in order to reduce computational cost. In brief, this method avoids calculation of $\lambda(z_b, l; t)$ for all values of z_b and l at each time t by selecting candidate eddies from a random distribution and estimating the value of λ only for a selected candidate, which is in turn randomly accepted at a small rate. This method generates correct results as long as the majority of the candidates are rejected, which is achieved by reducing Δt_{ODT} such that the average acceptance rate is limited to 0.05 (see details in Kerstein 1999).

2.3 The LES-ODT coupling

When coupled to the LES, ODT provides the full (resolved plus SGS) flow field within the lowest LES layer (of height Δz), which is identified as *ODT region* (red region in Fig. 1). This means that the variables $\widetilde{U}_1, \widetilde{U}_2$ and $\widetilde{\Theta}$ at $jz = 1$, in addition to $\widetilde{U}_3$ at $iz = 2$, are fully provided by ODT ($\widetilde{U}_3|_{iz=1} = 0$), in fact they are replaced by ODT values at each LES time-step (iz and jz are the indices for vertical positions in the code, see Fig. 1). In order to provide the ODT information in accordance with LES filtering, the ODT horizontal velocity and temperature vertical profiles are averaged over the LES time-step,

creating new variables $\widetilde{v}_1$, $\widetilde{v}_2$ and $\widetilde{\iota}$. The vertical velocity is calculated as

$$\widetilde{v}_3(z) = -\int_0^z \left(\frac{\partial \widetilde{v}_1}{\partial x} + \frac{\partial \widetilde{v}_2}{\partial y} \right) dz, \tag{14}$$

in order to preserve LES-level continuity. The LES horizontal components are then replaced by the average over Δz of their corresponding $\widetilde{v}_i$ ($\langle \widetilde{v}_i \rangle$, similarly for temperature $\langle \widetilde{\iota} \rangle$) as indicated in Fig. 1, whereas the vertical component is replaced by $\widetilde{v}_3$ at $iz = 2$, which guarantees continuity of the flow field.

In addition to the velocity and temperature fields, the SGS momentum and temperature fluxes (τ_{13}, τ_{23} and q_3) at the wall ($iz = 1$) are replaced by their corresponding ODT values τ^*_{13}, τ^*_{23} and q^*_3 (shear stress from the ODT wall model, heat flux imposed as constant). Their values at $iz = 2$, as well as τ_{33} at $jz = 1$, correspond to the total vertical ODT fluxes at the given position (t^*_{i3} and $t^*_{\theta 3}$, a sum of the contributions of stochastic eddies s^*_{i3} and $s^*_{\theta 3}$, vertical advection by $\widetilde{v}_3$ and SGS fluxes τ^*_{i3} and q^*_3 accumulated during the LES time-step, see Fig. 1), and are updated accordingly at each LES time-step. Because in this case the new LES SGS fluxes correspond to the total flux at $iz = 2$, the LES resolved vertical advective fluxes $\widetilde{u}_i\widetilde{u}_3$ and $\widetilde{\theta}\widetilde{u}_3$ are not required anymore and are therefore set to zero (see an example in the appendix of Freire and Chamecki (2021)).

Finally, ODT also provides to LES additional SGS fluxes from the stochastic eddies s^*_{i3} and $s^*_{\theta 3}$ in the *ODT overlap region* (from the top of the first LES cell to the middle of the fourth LES cell, see Fig. 1). In this region, the ODT velocity and temperature fields are constructed at each LES time-step as a linear interpolation of their respective LES vertical profiles. This additional domain allows *eddy events* to extend beyond Δz, as long as their bottom position is inside the *ODT region* ($z_b \leq \Delta z$). The vertical fluxes created by those eddies are then added to the LES SGS fluxes τ_{i3} and q_3 within the *ODT overlap region*, providing a better transition between the ODT eddies and the small resolved scales in LES. A sensitivity test for the size of the overlap region is provided by Schmidt et al. (2003) (reproduced by Freire and Chamecki (2021)).

The final step in this two-way coupling is the large-scale forcing of the ODT lines by LES-scale velocities. This is provided in two ways: (i) the flow field in the *ODT overlap region*, which is a linear interpolation of the LES field, is used as a top boundary condition in the *ODT region*; and (ii) the advection term in the ODT governing equations (6) and (7) uses $\widetilde{v}_i$ for advection, which are LES-scale velocities (they are in fact the LES velocities within the *ODT region*), coupling adjacent ODT domains.

To summarize, after defining initial values of $\widetilde{U}_i$, $\widetilde{\Theta}$, $\widetilde{u}_i$ and $\widetilde{\theta}$, the LES-ODT simulation is obtained by performing the following (within the LES time-step): (i) the calculation of the *ODT-overlap region* from the linear interpolation of the current LES field, and (ii) the evolution of the ODT flow field in smaller time-steps (using Eq. (6) and (7)), combined to the calculation of $\widetilde{v}_i$, $\widetilde{\iota}$ and the ODT vertical fluxes t^*_{i3}, $t^*_{\theta 3}$, s^*_{i3} and $s^*_{\theta 3}$ for that LES time-step. Then, the LES is advanced in time after incorporating the ODT values as listed in Fig. 1, and

finally a correction of the ODT velocity field is performed in order to rematch the LES after the imposition of the divergence-free condition (which changes all LES values, including those that came from ODT). More details of the correction and the overall coupling are provided by Schmidt et al. (2003) and Freire and Chamecki (2021).

3 Simulations

In order to test the LES-ODT ability to represent near-wall turbulence in the ABL, simulations of neutral, stable and unstable conditions were performed based on the study by Kleissl et al. (2006), which first tested a similar LES code using the MOST wall model. Simulations using both ODT and MOST were performed with the same LES parameters. The final computational cost of LES-ODT was about 4 times higher than LES-MOST for these simulations, which should be kept in mind when evaluating the cost-benefit of the results obtained here (the LES-MOST simulations took about 16 h to run, compared to about 60 h for the LES-ODT cases, both running in parallel using 32 processors). The impact of the ODT on the flow, as well as the statistics of the additional flow field provided by ODT, are presented in the next section.

Because ODT adds significantly to the overall computational cost, the test of a free-convection case was performed using fewer grid points in the LES-ODT simulation compared to LES-MOST. In this case, the work of Salesky and Anderson (2018) was used as a reference (which also used a similar LES code and the MOST wall model), where 256^3 grid points were used in a domain of $12\times12\times2$ km. For the LES-ODT simulation, $192\times192\times128$ grid points were used in a domain of $9\times9\times2$ km, which corresponds to the same horizontal resolution in a smaller domain, combined with a coarser vertical resolution in the same domain height (with a refined field near the wall provided by ODT). The new horizontal domain corresponds to a reduction from ~ 75 to ~ 56 integral length scales based on the streamwise behavior of the vertical velocity at $z/z_i \approx 0.1$. The integral length scale is in the order of z (Salesky et al. 2013), which is similar to the value estimated from the autocorrelation function up to the first zero crossing ($L_w^x \approx 160$ m). The reduction in vertical resolution allows the use of a doubled Δt, reducing by half the total number of time-steps required and the final computational cost of LES-ODT. In this free-convection case, the LES-MOST simulation took about 11 days to run, whereas LES-ODT needed around 6 days (both also running in 32 processors; note, however, that in the 256^3 simulation more processors could be used compared to the $192^2 \times 128$ case).

For all cases presented here, the minimum number of ODT grid points required for simulation convergence as obtained by Freire and Chamecki (2021) were used ($n_{\mathrm{ODT}} = 32$). Table 2 lists the simulation parameters. The initial condition was the geostrophic velocity plus random fluctuations in all three velocity components. The potential temperature profile was initiated with a constant value equal to 300 K up to the initial z_i, and a temperature inversion

Table 2 Simulation parameters. The neutral, stable and unstable cases were based on the study by Kleissl et al. (2006), and the free-convection case was based on Salesky and Anderson (2018). Parameters common to all simulations are $z_0 = 0.1, \Delta t = 0.4, N_t = 200\,000$ and total simulation time of 22h. All simulations were repeated for the MOST and ODT wall models. In the free-convection case, the MOST simulation had 256^3 grid points in a domain of $12 \times 12 \times 2$ km, requiring $\Delta t = 0.2$ and $N_t = 400\,000$ for the same total simulation time of 22h. Friction velocity at the wall estimated from the respective wall models. Surface temperature is estimated at the lowest LES grid point for consistency with LES-MOST. $L = -u_*^3 \theta_s / (\kappa g \overline{w'\theta'_s})$.

	neutral	stable	unstable	free-convection
domain size [km]		$2 \times 2 \times 1$		$9 \times 9 \times 2$
grid points ($nx \times ny \times nz, n_{\mathrm{ODT}}$)		$128 \times 128 \times 128, 32$		$192 \times 192 \times 128, 32$
geostrophic wind $\langle U_g, V_g \rangle$ [ms^{-1}]		$\langle 8, 0 \rangle$		$\langle 1, 0 \rangle$
Coriolis parameter f [s^{-1}]		1.45×10^{-4}		1×10^{-4}
initial z_i [km]		0.5		1
final z_i (approx.) [km]	0.5	0.16	0.58	1.2
surface heat flux $\overline{w'\theta'_s}$ [Kms^{-1}]	0	-0.02	0.1	0.24
final friction velocity u_* [ms^{-1}]	0.32	0.21	0.44	0.16
final surface temperature θ_s [K]	300.0	297.1	302.5	303.0
final Obukhov length L [m]	–	35.1	-65.7	-1.3

above it with strength of $0.05\,\mathrm{Km}^{-1}$ in the neutral/stable/unstable cases, and of $0.08\,\mathrm{Km}^{-1}$ up to 1100 m and $0.003\,\mathrm{Km}^{-1}$ above for the free-convection case. The ODT time-step remained at $\Delta t/15$ for all simulations tested here. All statistics presented next correspond to the horizontal and time average over the last 2 h of simulation (indicated by an overbar), except for the spectra, which use the streamwise information averaged over time and the y-direction, using three snapshots (at last time step, one hour before and two hours before the end of the simulation).

4 Results

4.1 Atmospheric stability tests

In this section we compare simulations of neutral, stable and unstable ABL between LES-ODT and LES-MOST using the same simulation parameters. Figure 2 shows an example of the additional near-wall flow field provided by ODT for the unstable case, which includes small-scale fluctuations from the stochastic turbulence model. On top of them, ODT extends the large-scale features already present in LES-MOST to the near-wall region. One way of visualizing this coupling is through the inclination angle of large-scale motions, as indicated in the figure. The inclination angle as a function of the atmospheric stability can be estimated as $\gamma(\zeta_z) = \tan^{-1}[\tan\gamma_0 + c_1 \kappa^{-1/3}(-\zeta_z)^{1/3}]$ (Salesky and Anderson 2020), in which $\gamma_0 \approx 12^{\mathrm{o}}$ is the inclination angle in neutral conditions, $c_1 = 0.569$ and $\zeta_z = z/L$ is the stability parameter (the lowest LES grid point height $z = 3.9$ m was used in the $\gamma(\zeta_z)$ estimation). This natural extension of the flow field was also obtained in the neutral and stable simulations, the former including the extension of the large-scale motions

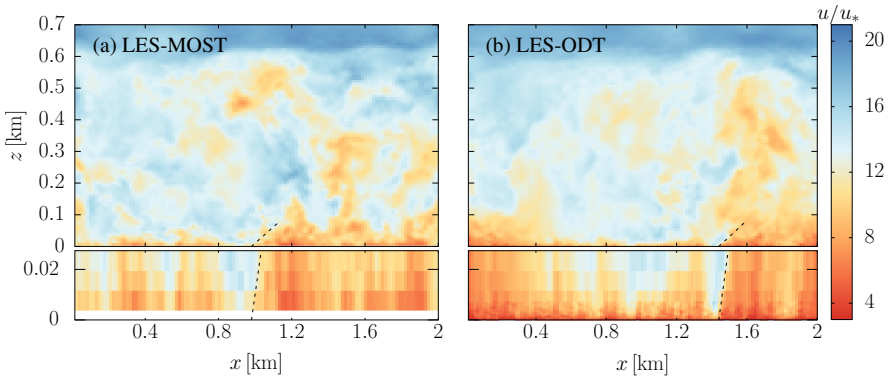

Fig. 2 Snapshots in the x–z plane of the streamwise velocity in the (a) LES-MOST and (b) LES-ODT simulations, for the unstable case, at the last simulation time-step. A closer look at the near-wall region is provided by the bottom plots, which show the ODT contribution to the flow field. Dashed lines correspond to the inclination angle $\gamma(z/L) = 27.3^{\text{o}}$, for $z = 3.9\,\text{m}$ (height of the lowest LES calculation).

with inclination angle $\gamma_0 \approx 12^{\text{o}}$ (not shown). Note that the choice of velocity threshold and location for coherent structure visualization is arbitrary, as it is used here only as a diagnostic tool rather than a proper study on inclination angle (the higher color contrast was chosen to facilitate the visualization).

One important impact of the ODT closure on the simulation is the early onset of turbulence compared to LES-MOST, due to the additional fluctuations in the near-wall region. For the cases tested here, LES-MOST developed fluctuations after ∼10 000 time-steps, instead of the first time-steps as observed in LES-ODT (see video in the supplemental material of Freire and Chamecki 2021). For that reason, there are some small differences in the flow statistics between the two models, as the turbulence development in the LES-ODT is always ahead of the LES-MOST but the forcing is the same, which impacts the overall evolution of the flow. This difference increases with instability due to the impact of turbulence intensity, and it can be noted, for example, in the mean velocity profiles of Fig. 3 (a), but note that the impact on the near-wall velocity gradient ϕ_m is smaller (Fig. 3 (b)). In future studies, this early onset of turbulence can be taken into account in order to reduce the total computational time required and consequently the overall cost of the simulation.

Figures 4–6 show the vertical profiles of velocity and temperature statistics for the neutral, unstable and stable cases, respectively. Overall, the results are similar to the LES-MOST simulations, and ODT provides the appropriate extension to the mean velocity and temperature profiles near the wall. The shear stress and heat flux exhibit the details of the coupling, which includes ODT providing the total values at $iz = 1$ and 2 ($\tau_{i3} = t^*_{i3}, q_3 = t^*_{\theta 3}$) and the additional flux from the stochastic eddies s^*_{i3} and $s^*_{\theta 3}$ in the ODT overlap region. Finally, as discussed in Freire and Chamecki (2021) and in several ODT stand-alone studies (e.g. Kerstein and Wunsch 2006; Freire and Chamecki 2018), the velocity variances from ODT are not exactly correct due to the

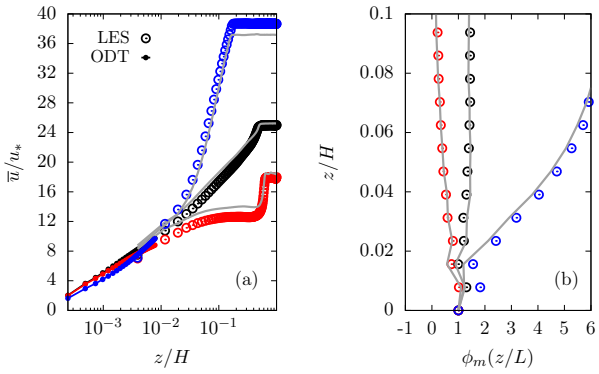

Fig. 3 (a) Mean velocity profiles and (b) non-dimensional velocity gradient functions $\phi_m(z/L)$, for neutral (black), stable (blue) and unstable (red) simulations (LES in open circles, ODT in closed circles). Grey lines are the corresponding LES-MOST results.

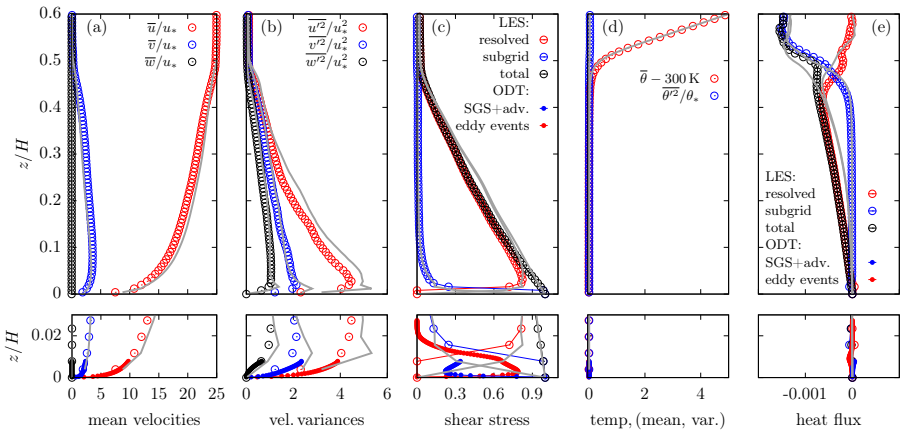

Fig. 4 Statistics of the velocity and temperature fields in the neutral simulation. (a) Mean velocities, (b) velocity variances, (c) shear stress ("adv." corresponds to the vertical advection by LES-scale velocity in ODT), (d) mean and variance of temperature and (e) heat flux. Circles for LES-ODT simulation (open circles LES, closed circles ODT) and gray lines for LES-MOST. The bottom plots show a closer look at the near-wall region. Velocity values are normalized by u_*, and temperature values are in [K] (mean), normalized by $\theta_* = \overline{w'\theta'_s}/u_*$ (variance) and in [Kms^{-1}] (heat flux).

stochastic nature of the turbulence model, but they provide an approximate estimation in terms of shape and order of magnitude.

One important impact of the ODT wall model is a reduction in the peak of the near-wall LES velocity variances, especially in the horizontal directions, for all stabilities (Figs. 4–6(b)). As discussed by Freire and Chamecki (2021), this reduction is likely an improvement in the LES results, since the one-dimensional spectra shows an elimination of a small "bump" and a behavior closer to the expected k_1^{-1} in the near-wall region (orange/red curves in Fig. 7,

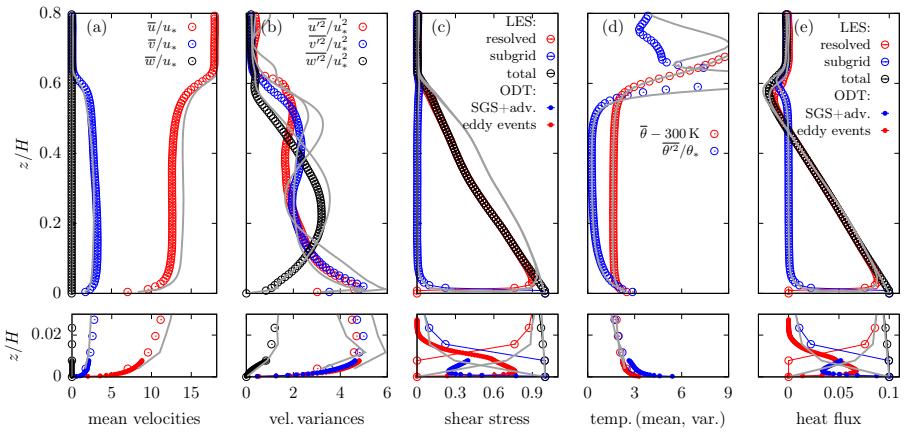

Fig. 5 Same as Fig. 4 for the unstable simulation.

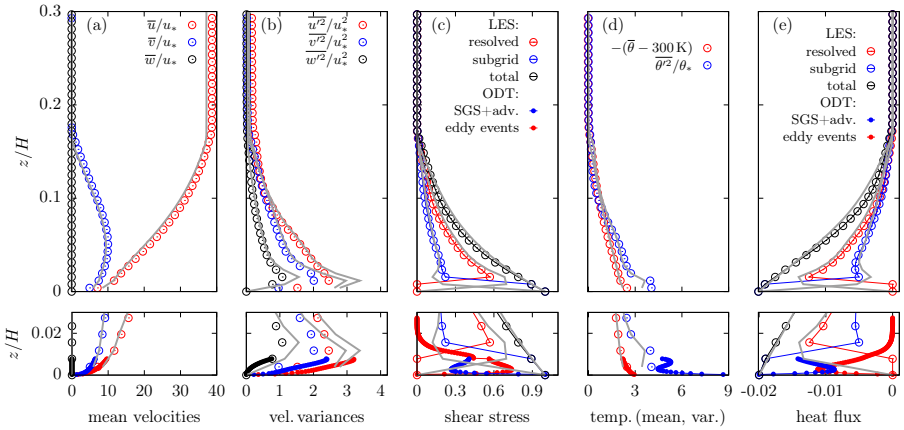

Fig. 6 Same as Fig. 4 for the stable simulation.

k_1 is the x_1 wavenumber). This impact extends to the overlap region, as indicated more clearly by the spanwise velocity spectra (Fig. 7(d),(e)), and it is less relevant in the stable case (right column of Fig. 7) due to its tendency on decoupling the bulk flow from the surface. Different from the channel flow cases of Freire and Chamecki (2021), the results here became slightly steeper than k^{-1}, likely caused by the Coriolis force implementation (which is the only significant difference between the neutral ABL and the channel flow cases, and it is also observed in rotating turbulence (Morize et al. 2005)). Furthermore, there is a degradation in the highest frequencies of the vertical velocity spectra (Fig. 7(g)–(i)), represented by an upward bending at the end of each line, which is likely related to the different treatment given to vertical velocity compared to the horizontal components in LES-ODT (the ODT vertical velocity

in LES-scale is not calculated from the vertical velocity in ODT-scale). Nevertheless, the overall result shows an improvement in the horizontal components that is likely related to the break-up and meandering of slightly smaller streaks caused by the stochastic nature of ODT, compared to the LES-MOST results (which has larger streaky structures in the spanwise direction, see Fig. 8). As discussed by Sagaut (2006, sec. 10.2.3), when grids are not refined enough, the formation of large spurious streaky structures can be observed, creating unphysical overshoot in turbulence intensities near the first grid point. It is possibly caused by a positive feedback between streaks and mean shear or by the impermeability constraint at the wall, and it can potentially be damped by adding a random noise (in this case provided by ODT). Finally, I note that the spectra provided by ODT at different heights present a similar behavior as the one shown in Fig. 7, but are omitted here for clarity in the presentation.

4.2 Free convection test

In this section, the free convection LES-MOST simulation of Salesky and Anderson (2018) is used as a reference, and a LES-ODT simulation with fewer grid points in each direction is tested. The effect of the domain and vertical resolution lost in the large-scale motion can be seen in Fig. 9 (a)–(d), which shows that although the intensity of the fluctuations presented some minor reduction, the overall large-scale structures were formed correctly.

Another relevant analysis in this case is a direct comparison between the information provided by ODT and the LES-MOST result at the same height. In Fig. 9 (e)–(f), which shows a top view of the vertical velocity fluctuations, the presence of large-scale structures similar to the ones observed in LES-MOST is noteworthy. Furthermore, the structures present in the streamwise velocity (Fig. 10) are extended to the near-wall region by ODT with a steep inclination angle, as predicted by the theory (Salesky and Anderson 2020).

The vertical profiles of flow statistics are provided in Fig. 11, where the same overall behavior obtained in the previous cases is observed. Figure 11(f) additionally shows the profile of vertical velocity skewness, which for LES-MOST has a spurious negative value in the near-wall grid points. This feature, common across different LES of the convective boundary layer, is likely caused by the SGS model (Schmidt and Schumann 1989) and is removed by the additional flow field provided by ODT. The one-dimensional spectra from LES-ODT, on the other hand, presents, for all variables, the same degradation observed previously only in the vertical velocity, characterized by an upward bending of each curve at their highest frequencies (Fig. 12). This degradation is likely caused by the increase in relative importance of the vertical velocity in the free convection case, and it is transferred to the overlap region. This degradation is likely not related to the reduction in domain/resolution, as it was not present in the LES-MOST simulation with this reduced setup (a LES-MOST simulation was also performed with the reduced domain/resolution, not shown). Nevertheless, except for this particular detail, the spectra in the ODT

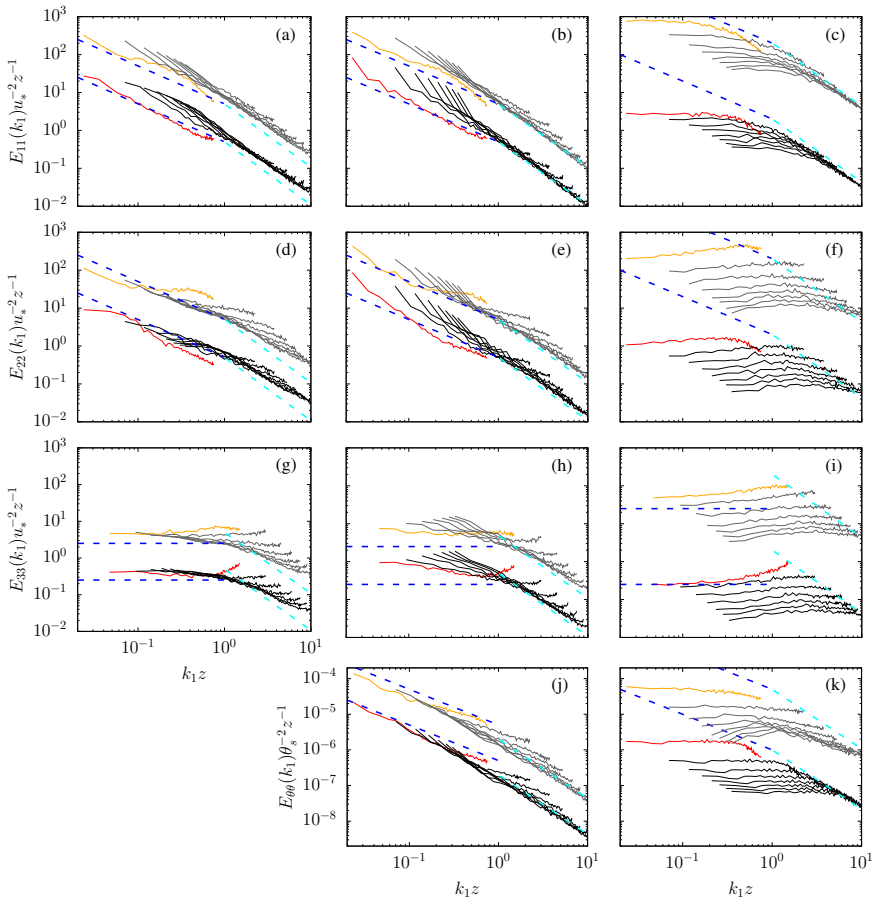

Fig. 7 One-dimensional spectra for velocity components u (a-c), v (d-f), w (g-i) and temperature (j,k) for the neutral (left column), unstable (mid-column) and stable (right column) simulations. Lines correspond to the lowest eight grid points in LES ($3.9 \leq z \leq 58.6$ m equally spaced by 7.8 m). LES-ODT in black/red and LES-MOST in grey/orange, vertically shifted by $\times 10$ (or $\times 100$ in the stable case). Red/orange lines correspond to the first LES grid point (obtained by ODT in the LES-ODT case). Blue and cyan lines indicate k_1^{-1} (or k_1^0 for the w plots) and $k_1^{-5/3}$, respectively.

region of the flow is similar to the LES-MOST spectra at the same height, a remarkable result given the idealized nature of the ODT turbulence model. Therefore, as observed in the previous cases, ODT can be used to provide a refined near-wall flow field with turbulence characteristics similar to that obtained by LES in the bulk of the flow.

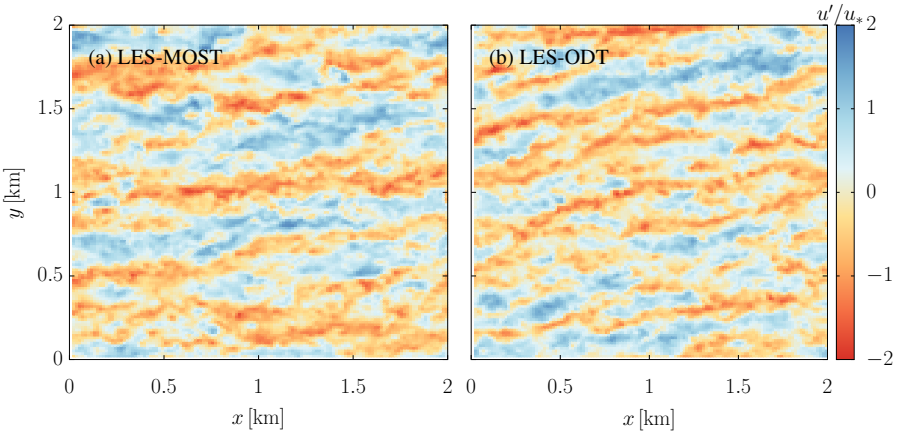

Fig. 8 Top-view snapshots of the neutral streamwise velocity fluctuation in the (a) LES-MOST and (b) LES-ODT simulations, at $z = 35.2$ m, from the last simulation time-step.

5 Conclusion

In this study, the LES-ODT model was tested for the simulation of the ABL under different stabilities. The code has been previously tested for channel flows (Freire and Chamecki 2021), demonstrating that it is robust for different Reynolds numbers and grid resolutions. Furthermore, it was shown that the code generates similar results when using the classical dynamic Smagorinsky subgrid-scale model in the LES (scale-invariant with planar averaging), which is also true for the ABL but it was not included here for brevity. Since it was demonstrated that the computational cost of LES-ODT is significantly higher than the LES-MOST (about 4 times higher for the cases tested here), a trade-off of lower LES resolution/domain size with more information in the near-wall region was tested for the free-convection case, providing a simulation with satisfactory results and similar computational cost.

Overall, for the same LES parameters, LES-ODT provides similar results to the LES-MOST, with small improvements of velocity variances in the LES near-wall region, reflected in both the one-dimensional spectra and in the breaking of large, likely spurious coherent structures. For all cases tested here (including the free-convection case with fewer LES grid points), the statistics of the additional near-wall flow provided by ODT were adequate for the mean velocity and temperature, shear stress and heat flux, with an approximate result (in terms of shape and order of magnitude) for the variances, an intrinsic characteristic of the ODT turbulence model. Nevertheless, the ODT provided similar spectra and extended the resolved turbulence and the large-scale structures of the LES to the near-wall region, correctly reflecting their statistics (such as the skewness of vertical velocity in the convective ABL) and inclination angle.

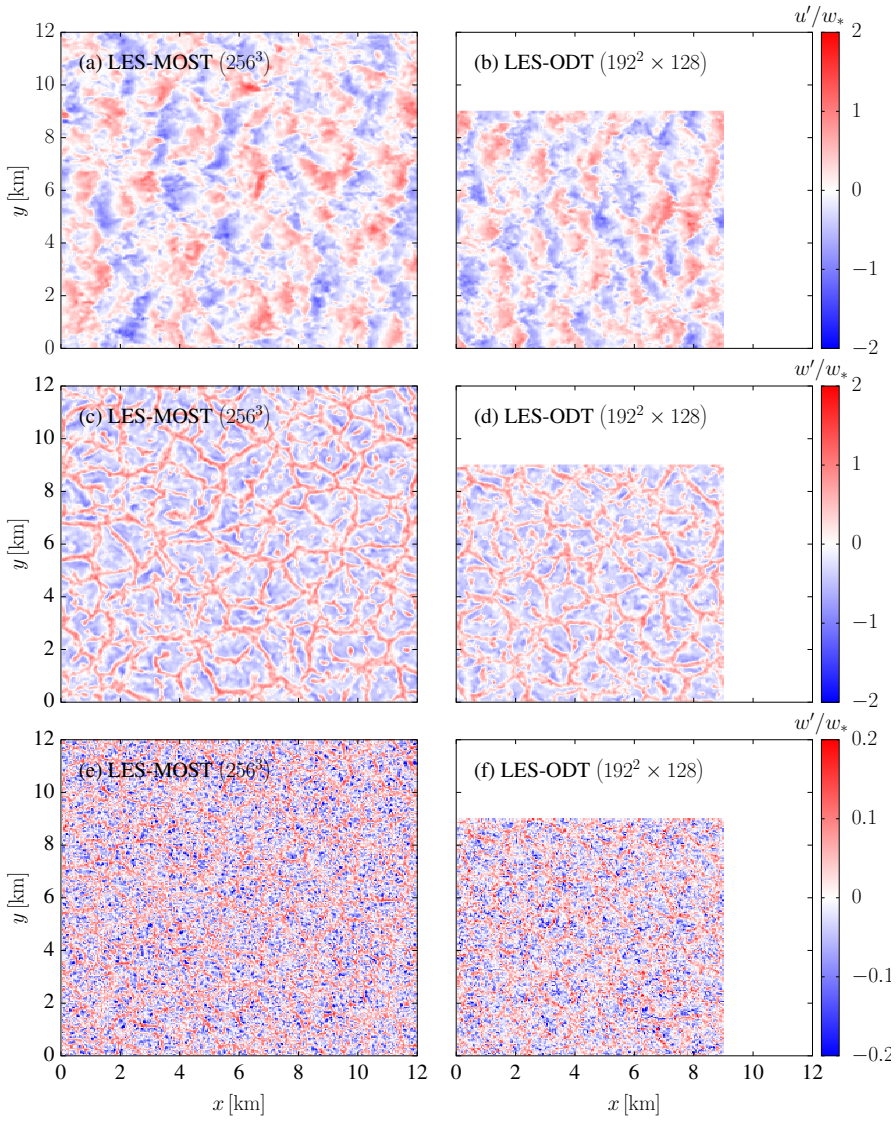

Fig. 9 Top-view of (a,b) streamwise and (c–f) vertical velocity fluctuations from a horizontal plane at (a–d) $z/z_i = 0.1$ and (e,f) $z/z_i = 0.01$, normalized by $w_* = (g\overline{w'\theta'_s} z_i/\theta_s)^{1/3} = 2.12\,\mathrm{ms}^{-1}$ (the Deardorff convective velocity scale), from the last simulation time-step. (a,c,e) LES-MOST with 256^3 grid points, and (b,d,f) LES-ODT with $192^2 \times 128$ grid points. For LES-ODT, (b,d) came from the LES part and (f) from the ODT part).

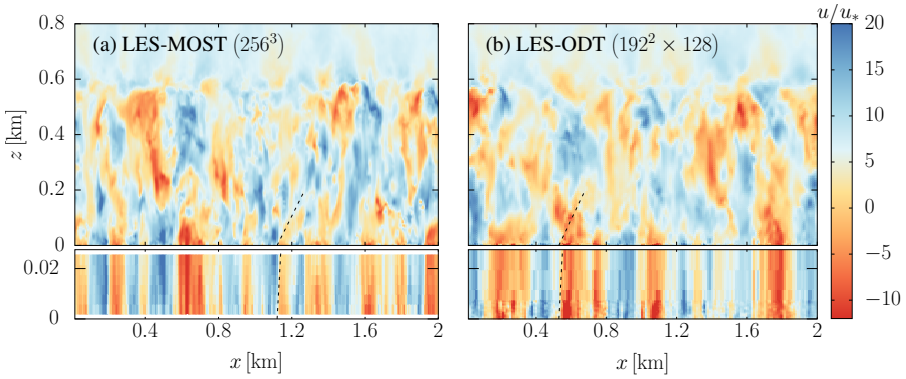

Fig. 10 Snapshots in the x–z plane of the streamwise velocity in the (a) LES-MOST and (b) LES-ODT simulations, for the free convection case, at the last simulation time-step. A closer look at the near-wall region is provided by the bottom plots, which show the ODT contribution to the flow field. Dashed lines correspond to the inclination angle $\gamma(z/L) = 53.0^{\circ}$, for $z = 3.9\,\mathrm{m}$.

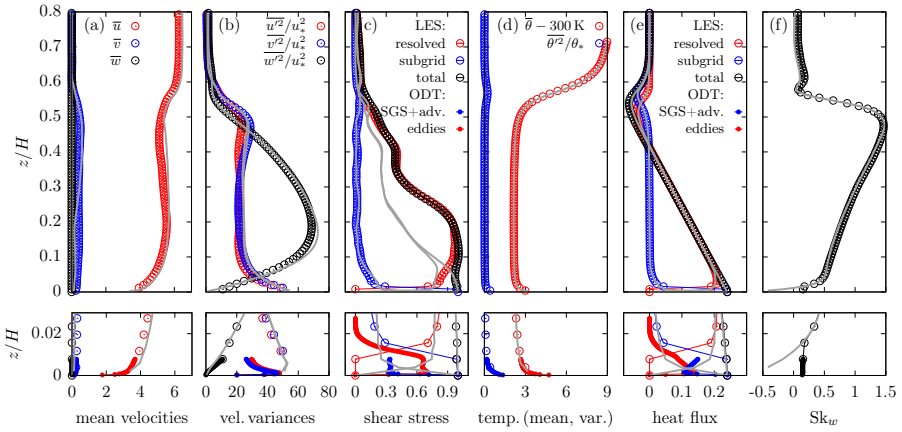

Fig. 11 From (a) to (e), same as Fig. 4 for the free-convection simulation. (f) Skewness of the vertical velocity.

Some insights regarding the trade-off between the near-wall resolution and the additional computational cost were given here, and it was demonstrated that the LES-ODT model can be a useful tool in the study of atmospheric boundary-layer problems with relevant near-wall phenomena. Examples of studies that can benefit from this model include the validity of MOST (as it is not invoked in LES-ODT), the *saltation* (jump) of sand particles (which causes dust emission) and the atmosphere-canopy interactions, since these problems can be highly impacted by large-scale structures reaching the ground. The code is particularly useful given that any additional Eulerian field, such as the concentration of gases and particles, can be directly incorporated with the same numerical treatment given here to the temperature. Furthermore, addi-

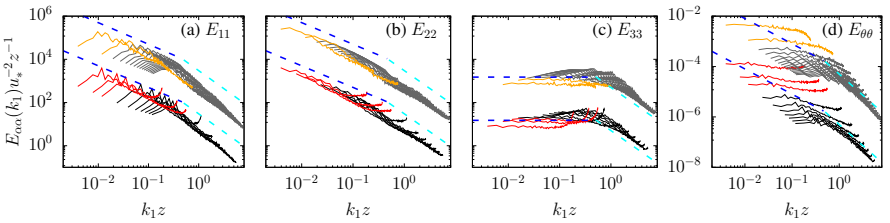

Fig. 12 One-dimensional spectra for velocity components (a) u, (b) v, (c) w and (d) temperature, for the free-convection simulation. LES-ODT in black/red and LES-MOST in grey/orange (vertically shifted by $\times 100$). For LES-MOST, lines correspond to the lowest sixteen grid points ($3.9 \leq z \leq 121.1$ m equally spaced by 7.8 m). For LES-ODT, lines correspond to the lowest eight LES grid points ($7.8 \leq z \leq 117.2$ m equally spaced by 15.6 m) plus two ODT grid points ($z = 3.9$ and 11.7). Red/orange lines correspond to the first two LES-MOST grid points and the LES-ODT results provided by ODT at the same height interval. Blue and cyan lines indicate k_1^{-1} (or k_1^0 for the w plot) and $k_1^{-5/3}$, respectively.

tional forces (such as the canopy drag force tested by Freire and Chamecki 2018, 2021) and sources/sinks of temperature and other scalars can be included in the same way as typically done in LES, expanding the applicability and potential of the tool.

Acknowledgements L.S.F. was funded by the São Paulo Research Foundation (FAPESP, Brazil), Grants No. 2018/24284-1 and 2019/14371-7. Research carried out using the computational resources of the Center for Mathematical Sciences Applied to Industry (CeMEAI) funded by FAPESP (grant 2013/07375-0). The author acknowledge the reviewers whose comments helped improve and clarify this manuscript. The datasets generated during and/or analysed during the current study are available from the corresponding author on reasonable request.

References

Andreotti B, Fourrière A, Ould-Kaddour F, Murray B, Claudin P (2009) Giant aeolian dune size determined by the average depth of the atmospheric boundary layer. Nature 457(7233):1120–1123, DOI 10.1038/nature07787

Bhuiyan MAS, Alam JM (2020) Scale-adaptive turbulence modeling for les over complex terrain. Engineering with Computers DOI 10.1007/s00366-020-01190-w

Bou-Zeid E, Meneveau C, Parlange M (2005) A scale-dependent lagrangian dynamic model for large eddy simulation of complex turbulent flows. Physics of Fluids 17(2):025105, DOI 10.1063/1.1839152

Chen B, Chamecki M, Katul GG (2019) Effects of topography on in-canopy transport of gases emitted within dense forests. Quarterly Journal of the Royal Meteorological Society 145(722):2101–2114, DOI 10.1002/qj.3546

Dupont S, Bergametti G, Marticorena B, Simoëns S (2013) Modeling saltation intermittency. Journal of Geophysical Research: Atmospheres 118(13):7109–7128, DOI 10.1002/jgrd.50528

Dupont S, Bergametti G, Simoëns S (2014) Modeling aeolian erosion in presence of vegetation. Journal of Geophysical Research: Earth Surface 119(2):168–187, DOI 10.1002/2013JF002875

Echekki T, Kerstein AR, Dreeben TD, Chen JY (2001) One-dimensional turbulence simulation of turbulent jet diffusion flames: model formulation and illustrative applications. Combustion and Flame 125(3):1083–1105, DOI 10.1016/S0010-2180(01)00228-0

Finnigan J (2000) Turbulence in plant canopies. Annual Review of Fluid Mechanics 32(1):519–571, DOI 10.1146/annurev.fluid.32.1.519

Freire LS, Chamecki M (2018) A one-dimensional stochastic model of turbulence within and above plant canopies. Agricultural and Forest Meteorology 250–251:9–23, DOI 10.1016/j.agrformet.2017.12.211

Freire LS, Chamecki M (2021) Large-eddy simulation of smooth and rough channel flows using a one-dimensional stochastic wall model. Computers & Fluids 230:105,135, DOI 10.1016/j.compfluid.2021.105135

Freire LS, Chamecki M, Gillies JA (2016) Flux-profile relationship for dust concentration in the stratified atmospheric surface layer. Boundary-Layer Meteorology 160(2):249–267, DOI 10.1007/s10546-016-0140-2

Giometto MG, Christen A, Meneveau C, Fang J, Krafczyk M, Parlange MB (2016) Spatial characteristics of roughness sublayer mean flow and turbulence over a realistic urban surface. Boundary-Layer Meteorology 160(3):425–452, DOI 10.1007/s10546-016-0157-6

Han BS, Baik JJ, Kwak KH, Park SB (2018) Large-eddy simulation of reactive pollutant exchange at the top of a street canyon. Atmospheric Environment 187:381 – 389, DOI 10.1016/j.atmosenv.2018.06.012

Kaimal JC, Finnigan JJ (1994) Atmospheric boundary layer flows: their structure and measurement. Oxford University Press

Kerstein A, Ashurst WT, Wunsch S, Nilsen V (2001) One-dimensional turbulence: vector formulation and application to free shear flows. Journal of Fluid Mechanics 447:85–109, DOI 10.1017/S0022112001005778

Kerstein AR (1999) One-dimensional turbulence: model formulation and application to homogeneous turbulence, shear flows, and buoyant stratified flows. Journal of Fluid Mechanics 392:277–334, DOI 10.1017/S0022112099005376

Kerstein AR, Wunsch S (2006) Simulation of a stably stratified atmospheric boundary layer using one-dimensional turbulence. Boundary-Layer Meteorology 118(2):325–356, DOI 10.1007/s10546-005-9004-x

Khanna S, Brasseur JG (1997) Analysis of monin–obukhov similarity from large-eddy simulation. Journal of Fluid Mechanics 345:251–286, DOI 10.1017/S0022112097006277

Khanna S, Brasseur JG (1998) Three-dimensional buoyancy- and shear-induced local structure of the atmospheric boundary layer. Journal of the Atmospheric Sciences 55(5):710 – 743, DOI 10.1175/1520-0469(1998)055¡0710:TDBASI¿2.0.CO;2

Klein M, Schmidt H (2018) Stochastic modeling of turbulent scalar transport at very high schmidt numbers. Proceedings in Applied Mathematics and Mechanics 17(1):639–640, DOI 10.1002/pamm.201710289

582 Klein M, Schmidt H, Lignell DO (2022) Stochastic modeling of surface scalar-
583 flux fluctuations in turbulent channel flow using one-dimensional turbu-
584 lence. International Journal of Heat and Fluid Flow 93:108,889, DOI
585 10.1016/j.ijheatfluidflow.2021.108889
586 Kleissl J, Kumar V, Meneveau C, Parlange MB (2006) Numerical study of
587 dynamic smagorinsky models in large-eddy simulation of the atmospheric
588 boundary layer: Validation in stable and unstable conditions. Water Re-
589 sources Research 42(6):W06D09, DOI 10.1029/2005WR004685
590 Kok JF, Parteli EJR, Michaels TI, Karam DB (2012) The physics of wind-
591 blown sand and dust. Reports on Progress in Physics 75(10):106,901, DOI
592 10.1088/0034-4885/75/10/106901
593 Morize C, Moisy F, Rabaud M (2005) Decaying grid-generated turbulence in
594 a rotating tank. Physics of Fluids 17(9):095,105, DOI 10.1063/1.2046710
595 Nieuwstadt FTM, Mason PJ, Moeng CH, Schumann U (1991) Large-eddy
596 simulation of the convective boundary layer – A comparison of four computer
597 codes. In: 8th Symposium on Turbulent Shear Flows, Volume 1, vol 1, pp
598 343–367
599 Pan Y, Chamecki M, Isard SA (2014) Large-eddy simulation of turbulence and
600 particle dispersion inside the canopy roughness sublayer. Journal of Fluid
601 Mechanics 753:499–534, DOI 10.1017/jfm.2014.379
602 Pan Y, Chamecki M, Isard SA, Nepf HM (2015) Dispersion of particles released
603 at the leading edge of a crop canopy. Agricultural and Forest Meteorology
604 211–212:37–47, DOI 10.1016/j.agrformet.2015.04.012
605 Rakhi, Klein M, M JAM, Schmidt H (2019) One-dimensional turbulence
606 modelling of incompressible temporally developing turbulent boundary
607 layers with comparison to dns. Journal of Turbulence 0(0):1–38, DOI
608 10.1080/14685248.2019.1674859
609 Richter DH, Dempsey AE, Sullivan PP (2019) Turbulent transport of spray
610 droplets in the vicinity of moving surface waves. Journal of Physical
611 Oceanography 49(7):1789 – 1807, DOI 10.1175/JPO-D-19-0003.1
612 Sagaut P (2006) Large Eddy Simulation for Incompressible Flows, 3rd edn.
613 Springer
614 Salesky ST, Anderson W (2018) Buoyancy effects on large-scale motions
615 in convective atmospheric boundary layers: implications for modulation
616 of near-wall processes. Journal of Fluid Mechanics 856:135–168, DOI
617 10.1017/jfm.2018.711
618 Salesky ST, Anderson W (2020) Revisiting inclination of large-scale motions
619 in unstably stratified channel flow. Journal of Fluid Mechanics 884:R5, DOI
620 10.1017/jfm.2019.987
621 Salesky ST, Katul GG, Chamecki M (2013) Buoyancy effects on the integral
622 lengthscales and mean velocity profile in atmospheric surface layer flows.
623 Physics of Fluids 25(10):105,101, DOI 10.1063/1.4823747
624 Schmidt H, Schumann U (1989) Coherent structure of the convective bound-
625 ary layer derived from large-eddy simulations. Journal of Fluid Mechanics
626 200:511–562, DOI 10.1017/S0022112089000753

627 Schmidt RC, Kerstein AR, Wunsch S, Nilsen V (2003) Near-wall LES closure
628 based on one-dimensional turbulence modeling. Journal of Computational
629 Physics 186(1):317–355, DOI 10.1016/S0021-9991(03)00071-8
630 Stoll R, Gibbs JA, Salesky ST, Anderson W, Calaf M (2020) Large-eddy sim-
631 ulation of the atmospheric boundary layer. Boundary-Layer Meteorology
632 177(2):541–581, DOI 10.1007/s10546-020-00556-3
633 Sullivan PP, Banner ML, Morison RP, Peirson WL (2018) Turbulent flow
634 over steep steady and unsteady waves under strong wind forcing. Journal of
635 Physical Oceanography 48(1):3 – 27, DOI 10.1175/JPO-D-17-0118.1
636 Sun G, Lignell DO, Hewson JC, Gin CR (2014) Particle dispersion in homo-
637 geneous turbulence using the one-dimensional turbulence model. Physics of
638 Fluids 26(26):103301, DOI 10.1063/1.4896555
639 Wurps H, Steinfeld G, Heinz S (2020) Grid-resolution requirements for large-
640 eddy simulations of the atmospheric boundary layer. Boundary-Layer Me-
641 teorology 175(2):179–201, DOI 10.1007/s10546-020-00504-1
642 Yang XIA, Park GI, Moin P (2017) Log-layer mismatch and modeling of the
643 fluctuating wall stress in wall-modeled large-eddy simulations. Phys Rev
644 Fluids 2:104,601, DOI 10.1103/PhysRevFluids.2.104601
645 Zhang Y, Hu R, Zheng X (2018) Large-scale coherent structures of suspended
646 dust concentration in the neutral atmospheric surface layer: A large-eddy
647 simulation study. Physics of Fluids 30(4):046,601, DOI 10.1063/1.5022089
648 Zhong J, Cai XM, Bloss WJ (2017) Large eddy simulation of reac-
649 tive pollutants in a deep urban street canyon: Coupling dynamics with
650 o3-nox-voc chemistry. Environmental Pollution 224:171 – 184, DOI
651 10.1016/j.envpol.2017.01.076